

# Improving the Performance of Vacuum-Deposited Perovskite Light-Emitting Diodes via a Tailored Sequential Deposition Strategy

Nakyung Kim,<sup>#</sup> Yunna Kim,<sup>#</sup> Jiyoung Kwon, Gui-Min Kim, Hee Joon Jung, Jinu Park, Sukki Lee, Seoyeon Park, Doh C. Lee, Yu-Ching Huang,\* and Byungha Shin\*



Cite This: *ACS Appl. Mater. Interfaces* 2025, 17, 56289–56298



Read Online

ACCESS |



Metrics & More



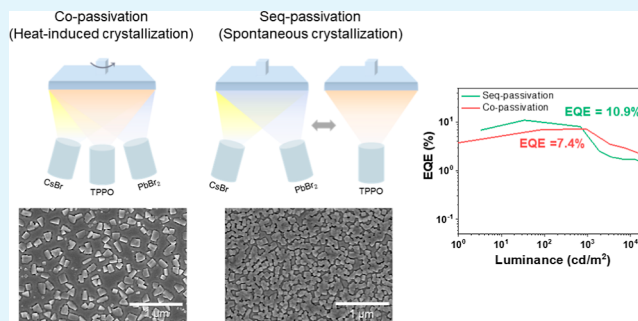
Article Recommendations



Supporting Information

**ABSTRACT:** Vacuum-deposited perovskite light-emitting diodes (PeLEDs) are attracting increased attention owing to their precise thickness control and absence of solvent-orthogonality constraints, offering significant potential for optimizing device performance. Here, we systematically compare how varying the deposition sequence of a single additive, triphenylphosphine oxide (TPPO)—known for its effective defect passivation—critically affects the crystallization dynamics, film morphology, and optoelectronic properties. Two distinct deposition strategies were compared: Co-passivation (simultaneous deposition of CsBr, PbBr<sub>2</sub>, and TPPO) and sequential-passivation (alternating ultrathin TPPO layers and perovskite layers). While Co-passivation delayed crystallization until annealing, sequential-passivation enabled partial crystallization during deposition, leading to smoother, more uniform films with higher photoluminescence quantum yield. Moreover, we demonstrate that TPPO induces quasi-2D perovskite formation, and to the best of our knowledge, this is the first report showing that a nonamine-based organic molecule induces quasi-2D formation. As a result, sequential-passivation devices achieved a higher external quantum efficiency (EQE) up to 10.9% and enhanced operational stability ( $T_{50} = 44$  min) compared to Co-passivation devices (EQE = 7.4%,  $T_{50} = 16$  min). This study highlights the importance of additive deposition sequence in determining the crystallization mechanism and optoelectronic properties of perovskite films, providing insights for designing high-performance vacuum-processed PeLEDs.

**KEYWORDS:** perovskites, light-emitting diodes, vacuum deposition, sequential passivation, sequential deposition, triphenylphosphine oxide



## 1. INTRODUCTION

Perovskite light-emitting diodes (PeLEDs) have gained significant attention as next-generation display materials due to their intrinsically narrow emission bandwidth (<20 nm, high color purity), compositionally tunable emission spanning the entire visible range, and relatively low fabrication cost.<sup>1–4</sup> Since the first report of PeLEDs with an external quantum efficiency (EQE) of only 0.1% in 2014,<sup>5</sup> intensive research has elevated device efficiencies to over 20% for red, green, and blue emitters.<sup>6–8</sup> To date, most research on PeLEDs has primarily relied on solution-based processing method. However, solution-based methods inherently face solvent-orthogonality constraints—each newly deposited layer should not dissolve the underlying layers.<sup>9–11</sup> Conversely, vacuum deposition methods circumvent solvent-orthogonality issues, enabling precise nanoscale thickness control and flexible deposition sequence adjustments. Such flexibility enables precise control over perovskite crystallization kinetics, thereby optimizing film morphology.<sup>12</sup>

Regardless of the deposition method, passivation strategies have been widely recognized as essential to improving PeLEDs performance by reducing trap states and suppressing non-

radiative recombination.<sup>13</sup> To effectively passivate defects within perovskite films, various Lewis base materials—including organic ammonium salts,<sup>14–17</sup> polymers,<sup>18,19</sup> and small organic molecules containing P=O groups,<sup>20,21</sup>—have been extensively investigated due to their strong binding affinity toward under-coordinated Pb<sup>2+</sup> centers, which mitigates deep trap states and enhances radiative recombination. Vacuum-deposited PeLEDs similarly benefit from passivation, employing methods such as coevaporation of passivation materials,<sup>22,23</sup> or sequential deposition of ultrathin passivation layers.<sup>24,25</sup>

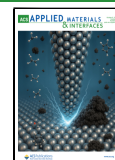
In addition to passivation, film morphology remains a critical determinant of PeLEDs performance. When employing passivation materials, it is crucial to consider their impact on morphology, as uniform films with smaller grain sizes

**Received:** June 22, 2025

**Revised:** September 15, 2025

**Accepted:** September 19, 2025

**Published:** September 30, 2025



significantly reduce leakage current and suppress nonradiative recombination, enhancing emission efficiency.<sup>26,27</sup> Recent vacuum-deposited PeLEDs studies have explored several strategies for morphology optimization, such as optimizing precursor ratios<sup>28,29</sup> and modulating the steric hindrance of underlying layers,<sup>30</sup> to achieve uniform, high-quality films. Nevertheless, systematic investigations comparing how the crystallization mechanism and film properties change based solely on the deposition sequence using the same additive have not yet been reported.

Furthermore, most vacuum-deposition-based perovskite studies have focused primarily on conventional three-dimensional (3D) bulk perovskite structures. In contrast, quasi-two-dimensional (quasi-2D) perovskite structures are receiving increasing attention because their quantum confinement and effective defect passivation properties can simultaneously enhance efficiency and stability.<sup>31,32</sup> However, large organic cations typically used to induce quasi-2D formation—such as phenethylammonium (PEA),<sup>33,34</sup> phenyltrimethylammonium (PTA),<sup>35</sup> phenylbutylammonium (PBA),<sup>36</sup> and butylammonium (BA)<sup>24,37</sup>—contain amine groups, making precise flux control challenging due to high volatility and poor thermal stability. Thus, developing new strategies employing vacuum-processable organic molecules without amine groups to form quasi-2D structures is needed.

In this study, we systematically investigated how the deposition sequence of a single additive—triphenylphosphine oxide (TPPO), known for its effective defect passivation ability and suitability for vacuum deposition process—influences the crystallization dynamics and optoelectronic properties of vacuum-deposited CsPbBr<sub>3</sub> perovskite films. We compared two deposition strategies: (i) Co-passivation, where CsBr, PbBr<sub>2</sub>, and TPPO are simultaneously deposited, and (ii) sequential-passivation, where ultrathin TPPO layers are deposited between thin (5 nm) perovskite layers. In Co-passivation, TPPO suppressed crystallization during deposition, inducing rapid and irregular grain growth upon annealing, which resulted in a nonuniform film. In contrast, the sequential-passivation method promoted partial crystallization in TPPO-free perovskite layers during deposition, exhibiting uniform grain growth upon annealing and significantly higher photoluminescence quantum yield (PLQY). Moreover, UV–VIS absorption and transient absorption spectroscopy revealed, for the first time, that TPPO induces quasi-2D perovskite formation, representing the first demonstration of quasi-2D structure formation using an organic molecule without amine functionality. As a result, sequential-passivation devices exhibited a higher external quantum efficiency of 10.9% compared to Co-passivation devices.

## 2. EXPERIMENTAL SECTION

**2.1. Materials and Chemicals.** Cesium bromide (CsBr, 99.999%), lead bromide (PbBr<sub>2</sub>, 99.999%), and triphenylphosphine oxide (TPPO, 98%) were purchased from Sigma-Aldrich. Poly(3,4-ethylenedioxythiophene)–poly(styrenesulfonate) (PEDOT:PSS, Al 4083), poly[*N,N'*-bis(4-butylphenyl)-*N,N'*-bisphenylbenzidine] (poly-TPD) were purchased from Heraeus, EMNI, respectively. 1,3,5-Tris(1-phenyl-1*H*-benzimidazol-2-yl)benzene (TPBi) and dipyrzino[2,3-*f*:2',3'-*h*]quinoxaline-2,3,6,7,10,11-hexacarbonitrile (HAT-CN) were purchased from Lumtec. All materials were used without any further processing.

**2.2. Preparation of the Perovskite Emitting Layer.** All perovskite films were deposited in a cryopump-equipped high-vacuum chamber ( $<3 \times 10^{-6}$  Torr). CsBr, PbBr<sub>2</sub>, and TPPO sources were

placed in separate pyrolytic boron nitride crucibles with high thermal conductivity, and the individual fluxes and thicknesses of each source were controlled by quartz crystal microbalance (QCM). During deposition, the substrate holder continuously rotated with a rotation speed of approximately 1 revolution per 23 s ( $\sim 2.6$  rpm) to ensure film uniformity, and the substrate temperature was maintained at room temperature. The target-to-substrate distance was fixed at 45 cm. After deposition, the samples were removed from the vacuum chamber and transferred to a dry room (relative humidity  $<2\%$ ), where they were annealed under controlled conditions.

**2.3. Fabrication of PeLEDs.** Glass substrates patterned with indium tin oxide (ITO) were successively cleaned in isopropanol, acetone, and deionized water for 15 min each, using sonication. The substrates were then dried under nitrogen flow and treated with UV–ozone for 15 min. A hole-injection layer of PEDOT:PSS was spin-coated at 4000 rpm for 40 s onto the UV–ozone-treated ITO and subsequently baked at 150 °C for 20 min. After annealing, the substrates were transferred into a nitrogen-filled glovebox, where p-TPD (10 mg/mL in chlorobenzene) was spin-coated at 3000 rpm for 50 s and then annealed at 100 °C for 10 min. The perovskite emissive layer was deposited in a dedicated vacuum chamber, followed by an additional annealing step. Subsequently, the samples were moved to an organic evaporator chamber, where 50 nm of TPBi, 1 nm of LiF, and 100 nm of Al were sequentially deposited. The effective device area, defined by the overlap of the ITO and Al electrodes, was 5 mm<sup>2</sup>.

**2.4. Characterizations and Measurements.** Thermogravimetric analysis (TGA) was performed using METTLER, TGA2 at KAIST Analysis Center for Research Advancement (KARA). The samples were heated in the range of 30–500 °C at the heating rate of 5 K/min in N<sub>2</sub> flow with an alumina crucible. Plan-view and tilted-view scanning electron microscope (SEM) images of the perovskite films were obtained using a Hitachi S4800 at 3 kV. The PLQY was obtained with a C13534-11 Quantaury-QY Plus UV-NIR absolute PLQY spectrometer (HAMAMATSU) under excitation wavelength of 370 nm. Grazing incidence X-ray diffraction (GIXRD) measurements were conducted using a Rigaku Ultima IV using Cu K $\alpha$  radiation ( $\lambda = 0.154$  nm) with an incident angle of 0.3° at KARA. The transmission electron microscope (TEM) samples were prepared by depositing a perovskite film on a SiN 5 nm TEM grid and imaged using a ThermoFisher scientific Technai G2 F30 at an 300 kV acceleration voltage. To determine the elemental composition of the perovskite and TPPO, a 1- $\mu$ m-thick perovskite film (maintaining the same stoichiometry as in the device) was deposited. The film was then mechanically scraped from the substrate to collect approximately 8 mg of powder for inductively coupled plasma mass spectrometry (ICP–MS) analysis. The obtained powder was digested in 200 °C of an acid solution (70% HNO<sub>3</sub> 3 mL + 35% HCL 1 mL) and analyzed using an ICP–MS instrument (ICAP-RQ, Thermo Fisher Scientific at KARA.) to quantify the relative amounts of Cs, Pb, and P. The Fourier transform infrared (FTIR) spectra were measured using a Nicolet iS50 instrument (Thermo Fisher Scientific) at KARA. Grazing-incidence wide-angle X-ray scattering (GIWAXS) measurements were performed at beamline 23A1 (BL 23A1) of the National Synchrotron Radiation Research Center (NSRRC) in Taiwan. The X-ray beam employed was monochromatic, with a photon energy set to 10 keV (wavelength: 1.2398 Å). To achieve sufficient penetration and effectively probe the thin films, the incidence angle was maintained at 0.2°. Wide-angle scattering data were collected using a flat-panel detector (C10158DK, 2352 pixels) positioned 17.25 cm away from the sample, with each measurement acquired over 60 s. Scattering intensity data underwent standard calibration procedures, including background subtraction, and results are expressed as scattering vector ( $Q$ ), defined as  $Q = 4\pi(\sin \theta)/\lambda$ , where  $\theta$  denotes half the scattering angle and  $\lambda$  represents the X-ray wavelength. The out-of-plane profiles were obtained by extracting intensity distributions perpendicular to the film and substrate surfaces from the two-dimensional GIWAXS patterns, whereas in-plane profiles were derived from intensity distributions parallel to the substrate. The time-resolved photoluminescence (TRPL) decay curves by fluorescence lifetime spectrometry (Fluorolog-QM, HORIBA) with an excitation wave-

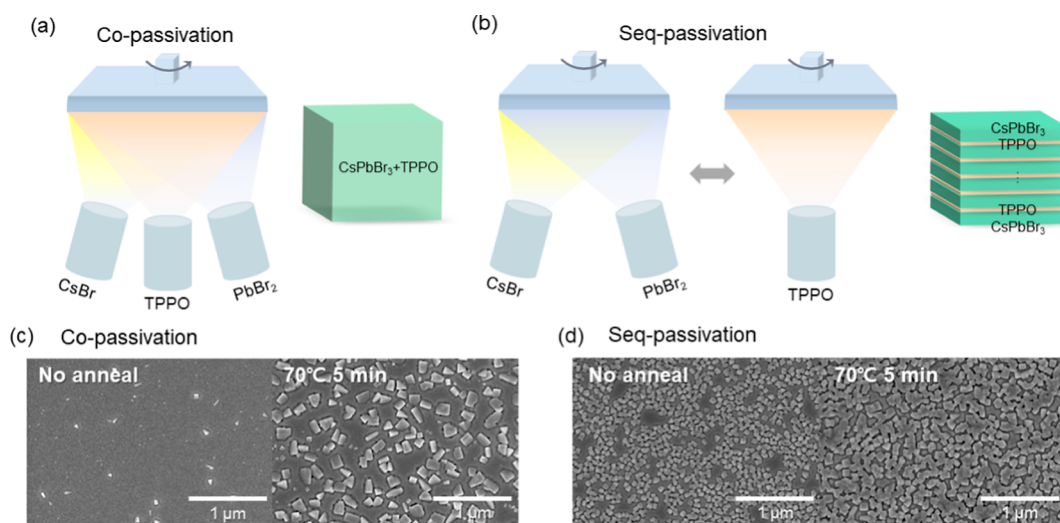


**Figure 1.** Schematic illustrations of (a) the Co-passivation and (b) the Seq-passivation. Top-view SEM images of (c) Co-passivation films and (d) Seq-passivation films before and after postdeposition annealing at 70 °C for 5 min.

length of 375 nm. The temperature-dependent PL spectra were also recorded by using the same equipment as TRPL, by varying the temperature from 77 to 300 K. The absorption spectra were measured using a UV-1800 UV-VIS spectrophotometer (SHIMADZU). Transient absorption (TA) measurements were performed on a 198 fs, 1028 nm femtosecond laser system (PHAROS, Light Conversion) operating at 200 kHz of repetition rate. This beam was used to seed an optical parametric amplifier equipped with a second harmonic module (ORPHEUS, Light Conversion) to produce the pump beam. The pump wavelength was tuned to 370 nm, and its power was attenuated to 1.0 mW with neutral density filter. The resulting beam radius was approximately 130  $\mu\text{m}$ . A portion of the fundamental beam served as the probe. It passed through a motorized delay line and was focused into sapphire to generate white-light continuum in a TA spectrometer (HARPIA, Light Conversion). The probe beam (with a beam radius of 105  $\mu\text{m}$ ) was then overlapped with the pump on the sample. The detector (Kymera 193i, Andor) was used to collect the probe beam that passed through the sample. The current density–voltage–luminance characteristics of the PeLEDs were measured using a Keithley 2635A source meter and a CS-2000 spectroradiometer, respectively.

### 3. RESULTS AND DISCUSSION

**3.1. Effect of Deposition Sequence on Film Morphology.** To assess the suitability of TPPO for thermal evaporation, we conducted thermogravimetric analysis (TGA) to evaluate the thermal stability of TPPO during perovskite film formation (Figure S1). A single-step decomposition began at around 300 °C, indicating that TPPO exhibits sufficiently robust thermal stability to withstand both thermal evaporation and subsequent annealing processes without degradation—an essential prerequisite for stable incorporation into vacuum-processed perovskite layers. Based on this stability, two distinct deposition processes were designed using the same perovskite precursor ratio ( $\text{CsBr}/\text{PbBr}_2 = 1.37:1.0$ ), but different TPPO insertion strategies (Figure 1a,b). Both deposition processes were conducted under Cs-rich conditions, setting CsBr and PbBr<sub>2</sub> flux rates at 0.48  $\text{\AA}/\text{s}$  and 0.35  $\text{\AA}/\text{s}$ , respectively, thereby maintaining a flux ratio greater than the stoichiometric unity. In this Cs-rich environment, the coexistence of Cs<sub>4</sub>PbBr<sub>6</sub> and CsPbBr<sub>3</sub> phases is known to enhance the PLQY.<sup>38,39</sup> The intended phase coexistence was confirmed through GIXRD analysis (Figure

S2). The first approach, referred to as Co-passivation, involves simultaneously depositing CsBr, PbBr<sub>2</sub>, and TPPO to form a 30 nm-thick film. In contrast, the Sequential-passivation (Seq-passivation) method alternates thin perovskite layers ( $\sim 5$  nm each) and ultrathin TPPO films, stacking them 6 cycles to achieve the desired total film thickness. In the Co-passivation process, TPPO was deposited at a flux rate of 0.06  $\text{\AA}/\text{s}$ , whereas in Seq-passivation, the TPPO layer thickness was precisely controlled at 0.9 nm. ICP–MS analysis indicated TPPO contents of approximately 20 at % and 70 at % for Co-passivation and Seq-passivation films, respectively (Table S1). These TPPO contents represent the optimized conditions for achieving maximum PLQY in each deposition method, and the detailed optimization processes will be discussed further in the following sections. This study optimized each deposition method to exhibit the highest efficiencies, enabling a comparative analysis of how deposition sequences impact film formation and characteristics.

The difference in film properties between the two deposition methods were evident from the films color observed immediately after deposition (Figure S3). Before annealing, the Co-passivation film was transparent without any observable PL emission under UV illumination, while the Seq-passivation film exhibited a pale-yellow film and weak PL emission. As the annealing time increased, both films turned deep yellow and exhibited strong PL under UV illumination. Consistent with this trend, the PLQY increased with annealing time, reached a maximum at 5 min, and then decreased (Figure S4). To further elucidate these differences, the film morphology evolution with annealing time was investigated (Figures 1c,d and S5). The Co-passivation films exhibited few perovskite crystallites before annealing, followed by rapid heat-induced crystallization when annealed at a mild temperature of 70 °C for 3 min. Conversely, Seq-passivation films showed partial spontaneous crystallization during deposition, forming uniform grain sizes even before annealing. Further annealing produced more homogeneous crystallite growth, resulting in highly uniform microstructures (Figure S6). Transmission electron microscopy (TEM) further highlighted differences in morphology between the two methods (Figure S7). After annealing, Co-passivation films exhibited numerous pinholes due to rapid crystallization, whereas Seq-passivation films showed densely packed grains

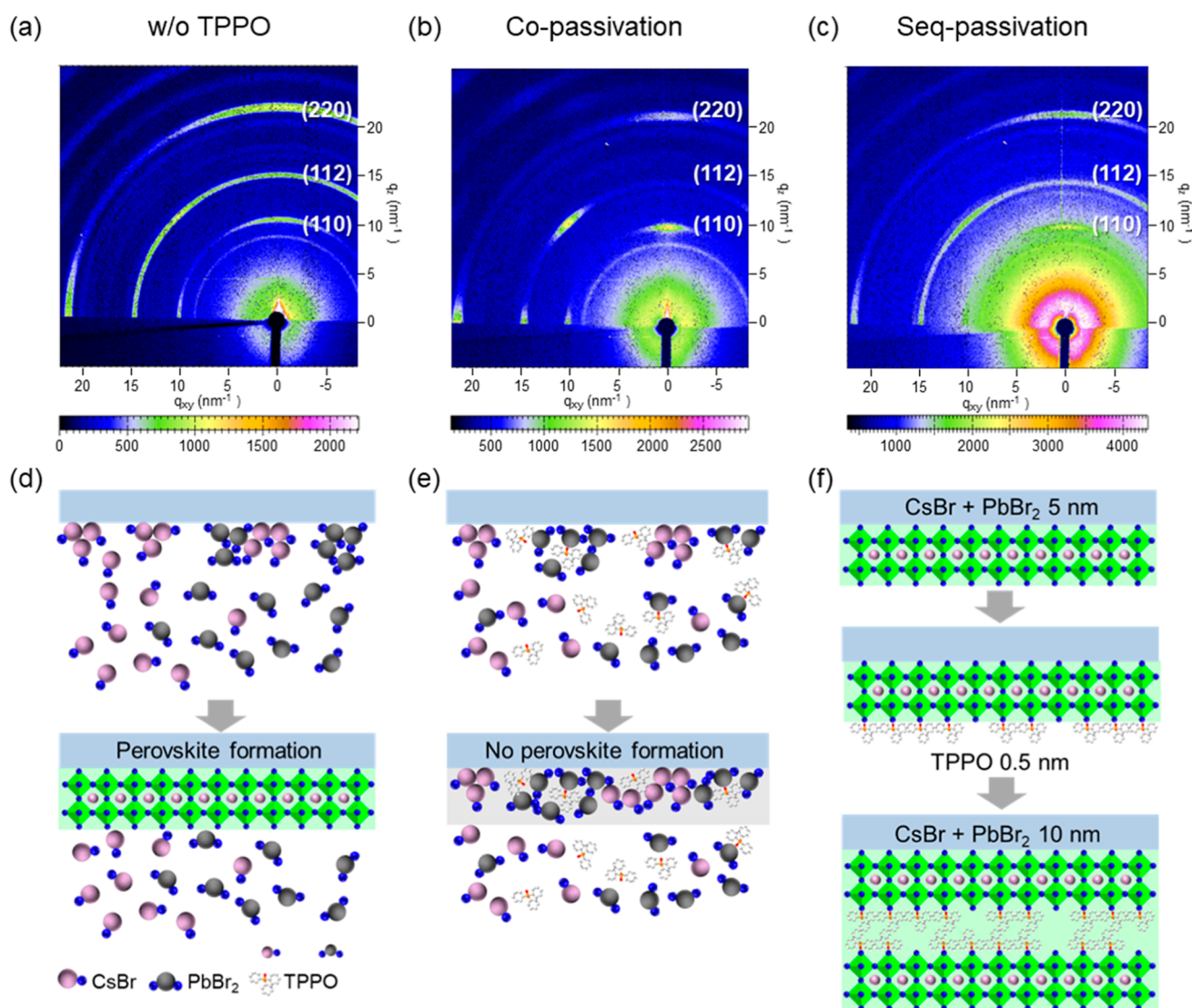


**Figure 2.** GIWAXS patterns of (a) pristine CsPbBr<sub>3</sub> (w/o TPPO), (b) Co-passivation, and (c) Seq-passivation perovskite films after annealing at 70 °C for 5 min. Schematics of the proposed mechanisms of perovskite growth in (d) w/o TPPO, (e) Co-passivation, and (f) Seq-passivation.

without significant pinholes. In addition, high resolution TEM of the Seq-passivation film further resolves the crystal lattice (Figure S8). Figure S8a shows a well-crystallized CsPbBr<sub>3</sub> region with only small defect regions (slight lattice displacement). Figure S8b presents a magnified view of the boxed area along the [100] zone axis, clearly revealing an orthorhombic unit cell. The measured lattice parameters ( $b = 8.25 \text{ \AA}$  and  $c = 11.78 \text{ \AA}$ ) are in good agreement with previously reported values. Atomic force microscopy (AFM) characterization shows that Seq-passivation films had significantly lower root-mean-square (RMS) roughness of 9.7 nm compared to 20.0 nm for Co-passivation films, confirming a smoother and more uniform surface (Figure S9). Reducing the annealing temperature to 50 °C for Co-passivation slightly lowered the RMS roughness to 18.6 nm, still notably higher than Seq-passivation (Figure S10). Thus, initiating nucleation at the deposition stage is crucial for achieving a uniform and smooth film. These morphological differences stemming from different TPPO insertion strategies are expected to significantly influence optoelectronic properties and device performance, which will be discussed in detail in the following.

**3.2. Effect of Deposition Sequence on Crystallization Dynamics.** To investigate the suppression of crystallization during deposition in the Co-passivation method, FTIR analysis was performed to compare the P=O stretching vibration peaks before and after annealing (Figure S11). A reference film composed of PbBr<sub>2</sub> and TPPO was prepared to examine the interaction between TPPO and PbBr<sub>2</sub>. In the Co-passivation sample, the P=O stretching vibration peak was observed at 1192 cm<sup>-1</sup> before annealing, identical to that of bare TPPO. However, after annealing, this peak shifted to 1185 cm<sup>-1</sup>, consistent with the peak position observed in the PbBr<sub>2</sub>-TPPO and Seq-passivation film. This shift indicates weakening of the P=O bond due to Lewis acid–base interaction between TPPO and Pb.<sup>21,22</sup> Thus, in the Co-passivation method, TPPO is predominantly bonded to PbBr<sub>2</sub>, likely hindering the initial reaction between CsBr and PbBr<sub>2</sub>. This is expected to delay nucleation of the perovskite phase and result in rapid heat-induced crystallization during the subsequent annealing process. On the other hand, since the Seq-passivation method initially deposits a layer without TPPO, perovskite films (5 and 30 nm thickness) without TPPO (w/o TPPO) was prepared for comparison (Figure S12). Tilted-view SEM images showed

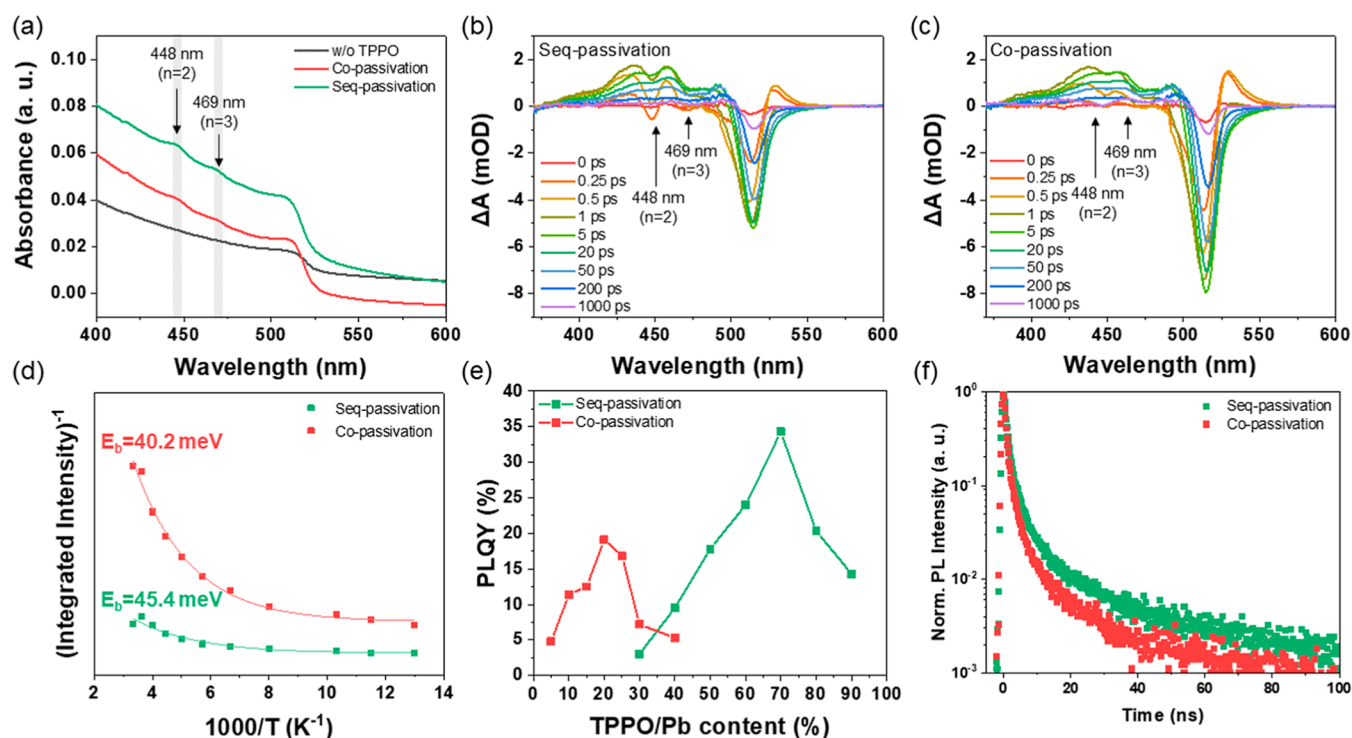


**Figure 3.** (a) UV–Vis absorption spectra of w/o TPPO, Co-passivation, and Seq-passivation films, exhibiting distinct peaks near 448 nm ( $n = 2$ ) and 469 nm ( $n = 3$ ) attributed to quasi-2D perovskite phases. Picosecond transient absorption (TA) spectra of (b) Seq-passivation and (c) Co-passivation. (d) Arrhenius plots of  $1/(\text{integrated PL intensity})$  vs  $1000/\text{temperature}$  (77–300 K) for Seq-passivation and Co-passivation films ( $E_b$  = Exciton-binding energies). (e) PLQY as a function of the TPPO/Pb content for both Co-passivation and Seq-passivation. (f) Time-resolved PL decay curves of Co-passivation and Seq-passivation.

that a uniform film was formed even at an ultrathin thickness of 5 nm for the w/o TPPO film, and it was confirmed that partial crystallization occurs before annealing at a thickness of 30 nm, growing more uniformly upon annealing. The morphological similarity between Seq-passivation and w/o TPPO films suggests that the initial crystallization critically influences the final film quality, and Seq-passivation films maintain the surface characteristics of the 5 nm w/o TPPO layer. GIWAXS analysis further supports that Seq-passivation films retain not only the morphological but also the crystallographic characteristics of the w/o TPPO films (Figures 2a–c and S13 and S14). In Co-passivation films, strong scattering patterns were observed at an azimuthal angle of  $90^\circ$  for the (110) plane ( $q = 10.7 \text{ nm}^{-1}$ ) and the (220) plane ( $q = 21.5 \text{ nm}^{-1}$ ), indicating preferential orientation. Additionally, intense scattering patterns at a  $45^\circ$  azimuthal angle were observed for the (112) plane ( $q = 15.2 \text{ nm}^{-1}$ ), consistent with the relative orientations of (110) and (220) planes to each other. In contrast, the w/o TPPO and Seq-passivation films showed broader scattering distributions for the (110) and (220) planes at  $90^\circ$ , indicating relatively random orientation. The (112) plane scattering was isotropic, further confirming random orientation in these films. Generally, the preferential orientation of the (110) plane facing the device thickness direction in perovskite films has been reported to enhance charge transport.<sup>40,41</sup> However, in this study, morphological uniformity and controlled grain size likely played a more significant role in enhancing the efficiency of Seq-passivation films, rather than crystal orientation alone. Overall, Seq-passivation maintained the morphological and crystallographic features from the initial deposition stage, whereas Co-

passivation demonstrated distinctly different crystallization behavior.

These crystallization mechanisms are illustrated schematically in Figure 2d–f. In the absence of TPPO, CsBr and PbBr<sub>2</sub> readily react during deposition to form a relatively uniform perovskite film, suggesting that Seq-passivation benefits from early stage crystallization and partial grain formation in a pure CsPbBr<sub>3</sub> layer. In contrast, Co-passivation allows TPPO to hinder early CsBr–PbBr<sub>2</sub> bonding, delaying crystallization until annealing, which can lead to uneven crystallization. Therefore, even with the same passivation additive, the deposition sequences and incorporation methods significantly impact perovskite crystallization behavior, film uniformity, and ultimately device performance.

### 3.3. Quasi-2D Perovskite Formation and Defect Passivation Effect.

UV–vis spectroscopy revealed significant differences in the absorption peaks of Co-passivation and Seq-passivation films, compared to the w/o TPPO films (Figure 3a). The main difference was the pronounced excitonic feature observed near the main absorption edge ( $\sim 515 \text{ nm}$ ) for Co-passivation and Seq-passivation films, indicating an increased exciton binding energy. This observation is consistent with their enhanced PLQY relative to the w/o TPPO film (Figure S15). Additionally, while the w/o TPPO films exhibited no distinct absorption peaks in the 400–500 nm range, the films containing TPPO displayed clear absorption peaks at 448 and 469 nm, corresponding to the characteristic peaks of  $n = 2$  and  $n = 3$  quasi-2D perovskite structures, respectively.<sup>38</sup> Quasi-2D perovskite structures not only have a high exciton binding energy due to quantum confinement effects, but also effectively passivate grain boundaries, suppressing nonradiative recombination and thereby extending carrier lifetimes.<sup>42,43</sup> TPPO, in

particular, is known for effective defect passivation material through the Lewis acid–base interaction between its P=O bond and Pb ions.<sup>21,22</sup> However, there have been no reports of TPPO inducing the formation of quasi-2D perovskite structures. Notably, this study is the first report to confirm quasi-2D perovskite formation with an organic molecule without having an amine group.

Transient absorption spectroscopy (TAS) further confirmed the formation of quasi-2D structures (Figure 3b,c). Ground state bleach (GSB) peaks corresponding to the  $n = 2$  and  $n = 3$  quasi-2D perovskite were observed, suggesting energy transfer pathways from quasi-2D to 3D bulk perovskite. Due to substantial overlap with strong photoinduced absorption (PIA) signals in the 400–500 nm range, accurately resolving the individual decay dynamics of the  $n = 2$  and  $n = 3$  GSB signals was not possible. Instead, we indirectly assessed energy transfer dynamics by analyzing the rise time of the 515 nm GSB peak corresponding to the 3D bulk perovskite (Figure S16). The rise times of the GSB peak in the Seq-passivation and Co-passivation films were similar at approximately 0.44 and 0.43 ps, respectively, nearly twice as long as that observed in the w/o TPPO film (0.21 ps), indicating the presence of energy transfer from quasi-2D to 3D bulk perovskite. This energy transfer from quasi-2D to 3D bulk increases the carrier density in the 3D bulk perovskite, rapidly saturating the trap states, which in turn effectively suppresses nonradiative recombination.<sup>33</sup> Additionally, both UV–vis and TAS spectra exhibited more pronounced quasi-2D absorption peaks in Seq-passivation films compared to Co-passivation films, which is likely due to the higher optimal TPPO content in the Seq-passivation method. UV–vis and TAS measurements were performed for the passivated films with varying TPPO contents (Figure S17). In the Co-passivation method, the absorption peaks corresponding to quasi-2D structures ( $n = 2$  and  $n = 3$ ) became stronger with increasing TPPO content from 20 at % to 30 at %. However, in the Seq-passivation method, increasing TPPO content beyond the optimal value (70 at %) required thicker TPPO layers, leading to local aggregation of TPPO, which inhibited further formation of quasi-2D structures (Figure S18).

Next, temperature-dependent PL measurement was conducted from 77 K to room temperature to estimate the exciton binding energy ( $E_b$ ) using the following equation (Figure 3d)

$$I(T) = \frac{I_0}{1 + A \exp(-E_b/k_B T)}$$

where  $I(T)$  is the temperature-dependent integrated PL intensity,  $I_0$  is the integrated PL intensity at 0 K, and  $k_B$  is the Boltzmann constant. The measured exciton binding energies were 45.4 and 40.2 meV for Seq-passivation and Co-passivation samples, respectively. Although these values are close to the typical exciton binding energy ( $\sim 40$  meV) of 3D CsPbBr<sub>3</sub> perovskites,<sup>16</sup> the slightly higher value observed for Seq-passivation films is likely due to the greater formation of quasi-2D perovskites formed by TPPO. This study demonstrates that organic molecules without amine groups, such as TPPO, can induce quasi-2D perovskite structures. However, the P=O bond of TPPO is relatively weak compared to the strong hydrogen bond provided by the amine group, resulting in limited quasi-2D formation. Nonetheless, these findings suggest the potential to achieve highly efficient vacuum-deposited quasi-2D perovskite formation using other vacuum-

processable organic molecules having stronger interactions with perovskite.

We then investigated how varying the TPPO content under each deposition strategy affects the PLQY (Figure 3e). The highest PLQY observed in Co-passivation was 19.1% at a TPPO/Pb ratio of approximately 20 at %, whereas Seq-passivation achieved a maximum PLQY of 34.3% at around 70 at %. In other words, the optimal Seq-passivation condition yielded a PLQY about 1.8 times higher than that of Co-passivation, with a TPPO/Pb ratio roughly 3.5 times greater. The higher PLQY observed in the Seq-passivation method can be attributed primarily to two factors. First, as confirmed by AFM and SEM analyses, Seq-passivation films exhibit lower RMS roughness and smaller grain sizes compared to Co-passivation films, resulting in fewer surface defects. We performed space-charge-limited current (SCLC) measurements using hole-only devices (HOD) with a structure of ITO/PEDOT:PSS/p-TPD/perovskites/HAT-CN/Al to quantitatively evaluate defect densities in the perovskite films (Figure S19). At low applied voltages, the current density showed a linear, ohmic relationship. With increasing voltage, the current density rises rapidly, reflecting the filling of trap states within the films. The voltage at which this transition occurs is known as the trap-filled limited voltage ( $V_{TFL}$ ), which directly correlates to the trap density in the material according to the equation,  $V_{TFL} = qn_t L^2 / 2\epsilon\epsilon_0$ , where  $q$  is the elementary charge,  $n_t$  is the trap density,  $L$  is the film thickness,  $\epsilon$  is the relative dielectric constant, and  $\epsilon_0$  is the vacuum permittivity.<sup>44</sup> The Seq-passivation films exhibited significantly lower  $V_{TFL}$  values compared to Co-passivation films, confirming their reduced trap density from  $3.72 \times 10^{18} \text{ cm}^{-3}$  to  $1.48 \times 10^{18} \text{ cm}^{-3}$ . This result aligns well with the smoother morphology observed in Seq-passivation films, thereby corroborating the superior defect passivation and higher PLQY achieved by the sequential deposition strategy. Second, the greater formation of quasi-2D perovskites in Seq-passivation films enhances the grain boundary passivation effect, effectively reducing nonradiative recombination. Initially, we anticipated that increasing TPPO content would promote more extensive quasi-2D formation, thereby enhancing defect passivation. However, in the Co-passivation approach, exceeding a TPPO/Pb ratio of 20 at % resulted in a decrease in PLQY. This reduction is likely due to excessive TPPO interfering with the initial reaction between CsBr and PbBr<sub>2</sub>, thus further hindering perovskite crystallization. In contrast, the Seq-passivation method introduces TPPO as ultrathin interfacial layers, allowing perovskite crystallization to proceed continuously during deposition. Therefore, Seq-passivation enables effective crystallization and passivation even at higher TPPO contents, with PLQY peaking at a TPPO content of 70 at %. However, excessively thick TPPO layers led to aggregation, which reduced the overall passivation efficiency, making the 70 at % condition optimal. To better understand how the individual layer thickness and deposition cycles of TPPO layers influence passivation efficiency in Seq-passivation, additional experiments were performed at a fixed TPPO content of 70 at % (Figure S20). Specifically, we compared two conditions with identical total thicknesses but different layering schemes: (i) perovskite layers of 3 nm repeated 10 times (total 30 nm) alternating with TPPO layers of 0.5 nm repeated 9 times (total 4.5 nm), and (ii) perovskite layers of 10 nm repeated 3 times (total 30 nm) alternating with TPPO layers of 2.25 nm repeated 2 times (total 4.5 nm). Both conditions resulted in

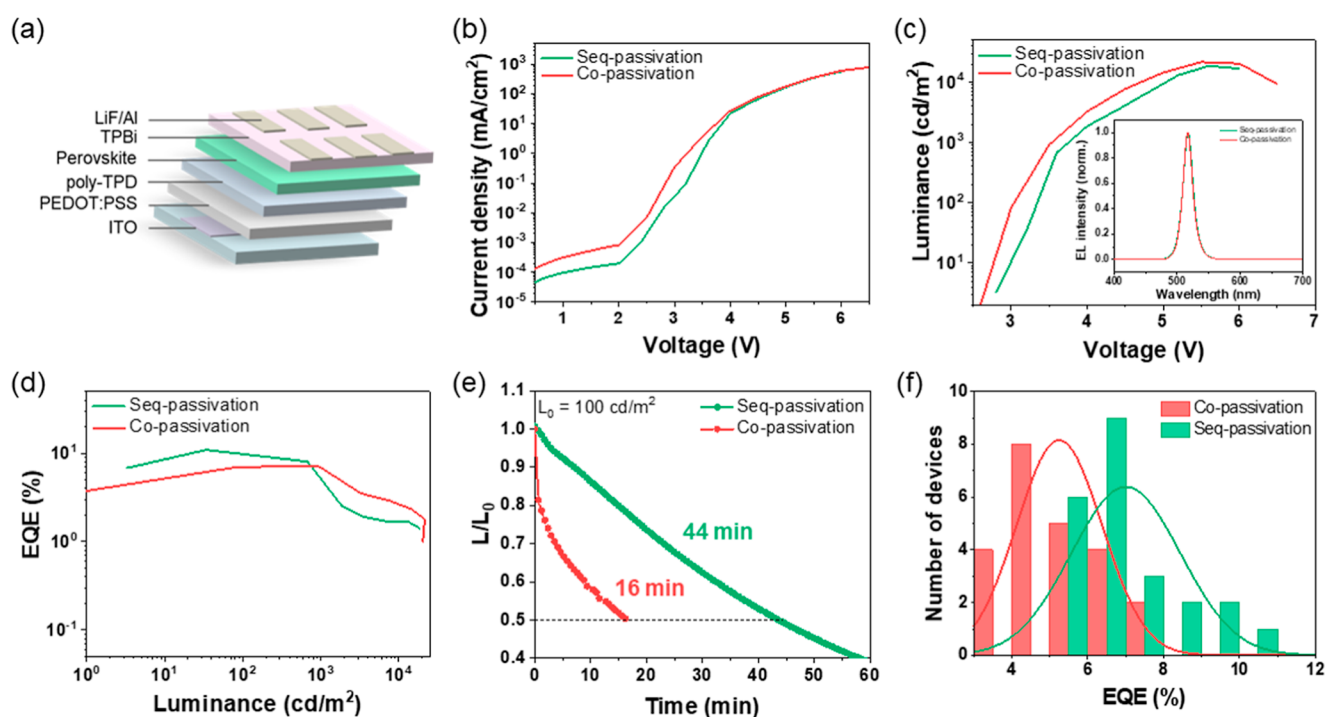


**Figure 4.** (a) Schematic illustration of the PeLEDs device architecture. (b) Current density–voltage ( $J$ – $V$ ). (c) Luminance–voltage (inset: normalized EL spectra of Seq-passivation and Co-passivation), (d) external quantum efficiency–luminance characteristics of Seq-passivation and Co-passivation devices. (e) Operational stability at  $L_0$  100  $\text{cd/m}^2$ . (f) Peak EQE histogram over 20 devices of Seq-passivation and Co-passivation devices.

lower PLQY compared to the optimal 5 nm perovskite layers and 0.9 nm TPPO layers repeated 5 times. In the former case, the ultrathin (0.5 nm) TPPO layers likely failed to fully cover the interfaces uniformly, compromising the passivation effectiveness. In the latter case, the reduced number of deposition cycles decreased the total fraction of perovskite volume effectively passivated at each interface, diminishing the overall passivation effectiveness and thereby lowering the PLQY.

Transient-resolved PL (TRPL) measurements also revealed that Seq-passivation films exhibited longer average carrier lifetimes and effectively suppressed nonradiative recombination compared to Co-passivation films (Table S2). Additionally, fitting the 77 K PL spectra using a Voigt function showed that Seq-passivation films produced a single, clean emission peak centered at approximately 520 nm (Figure S21). In contrast, Co-passivation films exhibited a primary emission peak at around 522 nm with an additional shoulder at about 530 nm, indicative of shallow trap states located 35–40 meV below the conduction band edge. Considering that thermal energy ( $k_B T$ ) at room temperature is  $\sim 26$  meV, these shallow traps could potentially be thermally deactivated under operating conditions, somewhat mitigating their detrimental effects. Nevertheless, the absence of subgap emission in Seq-passivation films even at low temperatures confirms that both interior and interfacial defects were effectively suppressed starting from the early stages of crystallization. In summary, the Seq-passivation method facilitates initial crystallization during deposition, allowing sufficient incorporation of TPPO. This approach resulted in uniform films and enhanced quasi-2D perovskite formation, leading to effective defect passivation and significantly improved PLQY.

**3.4. Device Performances.** To assess how the high PLQY and effective defect passivation observed in the Co- and Seq-passivation films translate into actual LED device performance, we fabricated PeLEDs with a device structure of ITO/PEDOT:PSS/p-TPD/perovskite (Co-passivation or Seq-passivation)/TPBi/LiF/Al (Figure 4a). Using identical electrode and charge-transport layers, we varied only the perovskite emissive layer (deposited via either Seq- or Co-passivation), and compared their current density–voltage–luminance ( $J$ – $V$ – $L$ ) and EQE–luminance characteristics (Figure 4b–d). Seq-passivation devices exhibited higher shunt resistance than Co-passivation devices, likely due to their smoother and more uniform surface morphology. However, Seq-passivation devices also showed increased series resistance, likely related to their higher TPPO content. This is consistent with the results in Figure S22, which showed that higher TPPO concentrations led to a decrease in current density. Despite the slightly reduced current injection at the same voltage, Seq-passivation devices achieved a higher record external quantum efficiency (EQE) of 10.9%, compared to 7.4% for Co-passivation devices, owing to their higher PLQY. Notably, as shown in Figure S23, the current densities of HOD and electron-only devices (EOD, ITO/TPBi/perovskites/TPBi/LiF/Al) for Seq-passivation were similar across the applied voltage range. This balanced charge injection resulted from the higher TPPO content in Seq-passivation films, which reduces hole injection relative to electron injection, thereby improving overall charge balance and enhancing EQE. At low voltages ( $< 4$  V), Co-passivation devices displayed higher current injection characteristics and higher luminance due to their lower series resistance. However, as voltage increased, the differences in current density and luminance between the two devices gradually diminished. Although increasing quasi-2D structures typically reduces

charge injection, TPPO, which is composed of three conducting benzene rings, allows more efficient charge injection compared to other organic spacers with alkyl groups. As a result, even with 70% TPPO content, charge injection remains more efficient. The Seq-passivation devices reached a maximum luminance of 18,611 cd/m<sup>2</sup> at 5.6 V, whereas the Co-passivation devices achieved a slightly higher maximum luminance of 21,676 cd/m<sup>2</sup> at 5.5 V. Both devices exhibited similar electroluminescence (EL) spectra, featuring an EL peak at 518 nm and a full-width at half-maximum (fwhm) of 19 nm (Figure 4c). Detailed device performance data across varying TPPO concentrations for each deposition method are summarized in Table S3. We further evaluated operational stability by driving at constant current conditions under an initial luminance of 100 cd/m<sup>2</sup> (Figure 4e). The device lifetime, defined as the time required for the luminance to decrease by half ( $T_{50}$ ), was found to be 44 min for Seq-passivation and 16 min for Co-passivation, demonstrating superior stability for Seq-passivation devices. Finally, Figure 4f presents histograms of EQE distributions measured from 20 devices fabricated using each deposition method. Seq-passivation devices exhibited higher peak EQE (10.9%) and average EQE (7.0%), compared to Co-passivation devices with comparatively lower peak (7.4%) and average (5.2%) EQEs. These results highlight that even with identical TPPO additives, differences in deposition sequence and insertion method can substantially influence interface defect control and radiative recombination efficiency.

#### 4. CONCLUSIONS

In conclusion, we systematically investigated how deposition sequence of perovskite emitter and passivation additives critically influences the crystallization behavior and optoelectronic properties of vacuum-deposited CsPbBr<sub>3</sub> films. Co-passivation (simultaneous deposition of CsBr, PbBr<sub>2</sub>, and TPPO) resulted in nonuniform films due to delayed crystallization followed by rapid grain growth during annealing. In contrast, Seq-passivation (alternating TPPO and perovskite layers) enabled spontaneous crystallization during deposition, yielding uniform grain sizes and significantly improved film quality. Moreover, we demonstrated that TPPO—an organic molecule without amine functionality—can induce quasi-2D perovskite formation. However, the weaker interaction of TPPO compared to amine-based hydrogen bonding limited extensive quasi-2D formation. Ultimately, Seq-passivation devices achieved an external quantum efficiency (EQE) of up to 10.9% with enhanced operational stability. These findings emphasize the critical role of deposition sequence in controlling crystallization and optimizing film properties, providing insights for designing efficient vacuum-processed PeLEDs. Furthermore, developing vacuum-compatible organic molecules featuring stronger intermolecular interactions similar to amine-based hydrogen bonds could further improve device performance.

#### ■ ASSOCIATED CONTENT

##### SI Supporting Information

The Supporting Information is available free of charge at <https://pubs.acs.org/doi/10.1021/acsami.5c12257>.

TGA curves; GIXRD curves; ICP-MS results; top-view SEM images; plan-view TEM images; AFM topography images; FTIR spectra; GIWAXS line-cut profiles; PL

spectra; UV-vis spectra; TAS spectra; SCLC curves; summary of device performance (PDF)

#### ■ AUTHOR INFORMATION

##### Corresponding Authors

**Yu-Ching Huang** – Department of Materials Engineering, Ming Chi University of Technology, New Taipei City 243303, Taiwan; [orcid.org/0000-0003-4772-8050](https://orcid.org/0000-0003-4772-8050); Email: [huangyc@mail.mcut.edu.tw](mailto:huangyc@mail.mcut.edu.tw)

**Byungha Shin** – Department of Materials Science and Engineering, Korea Advanced Institute of Science and Technology (KAIST), Daejeon 34141, Republic of Korea; [orcid.org/0000-0001-6845-0305](https://orcid.org/0000-0001-6845-0305); Email: [byungha@kaist.ac.kr](mailto:byungha@kaist.ac.kr)

##### Authors

**Nakyung Kim** – Department of Materials Science and Engineering, Korea Advanced Institute of Science and Technology (KAIST), Daejeon 34141, Republic of Korea

**Yunna Kim** – Department of Materials Science and Engineering, Korea Advanced Institute of Science and Technology (KAIST), Daejeon 34141, Republic of Korea; [orcid.org/0009-0004-2875-3052](https://orcid.org/0009-0004-2875-3052)

**Jiyoung Kwon** – Department of Materials Science and Engineering, Korea Advanced Institute of Science and Technology (KAIST), Daejeon 34141, Republic of Korea

**Gui-Min Kim** – Department of Chemical and Biomolecular Engineering, Energy and Environmental Research Center (EERC), KAIST Institute for NanoCentury (KINC), KAIST Graduate School of Semiconductor Technology, Korea Advanced Institute of Science and Technology (KAIST), Daejeon 34141, Republic of Korea

**Hee Joon Jung** – Emerging Material Metrology Group, Division of Chemical and Material Metrology, Korea Research Institute of Standards and Science (KRISS), Daejeon 34113, South Korea

**Jinu Park** – Department of Materials Science and Engineering, Korea Advanced Institute of Science and Technology (KAIST), Daejeon 34141, Republic of Korea; [orcid.org/0000-0001-7307-8456](https://orcid.org/0000-0001-7307-8456)

**Sukki Lee** – Department of Materials Science and Engineering, Korea Advanced Institute of Science and Technology (KAIST), Daejeon 34141, Republic of Korea

**Seoyeon Park** – Department of Materials Science and Engineering, Korea Advanced Institute of Science and Technology (KAIST), Daejeon 34141, Republic of Korea

**Doh C. Lee** – Department of Chemical and Biomolecular Engineering, Energy and Environmental Research Center (EERC), KAIST Institute for NanoCentury (KINC), KAIST Graduate School of Semiconductor Technology, Korea Advanced Institute of Science and Technology (KAIST), Daejeon 34141, Republic of Korea; Center of Excellence on Catalysis and Catalytic Reaction, Department of Chemical Engineering, Faculty of Engineering, Chulalongkorn University, Bangkok 10330, Thailand; [orcid.org/0000-0002-3489-6189](https://orcid.org/0000-0002-3489-6189)

Complete contact information is available at: <https://pubs.acs.org/doi/10.1021/acsami.5c12257>

##### Author Contributions

#N.K. and Y.K. contributed equally to this work. N.K. and Y.K. performed the experiments, including LED device fabrication

and data analysis, and cowrote the manuscript. J.K. and H.J.J. performed SEM and TEM measurements and analyzed the respective data. G.-M.K. and D.C.L. carried out TAS measurements and analyzed the results. J.P., S.L., and S.P. conducted PLQY, TRPL, and TDPL measurements and analyzed the data. Y.-C.H. performed GIWAXS measurements and analyzed the results. B.S. supervised the project and reviewed the manuscript. All authors discussed the results and contributed to the final revision of the manuscript.

## Notes

The authors declare no competing financial interest.

## ACKNOWLEDGMENTS

This work was supported by the National Research Foundation of Korea (NRF) grant funded by the Korea government (MSIT) (RS-2022-NR068162, RS-2023-00208832).

## REFERENCES

- (1) Quan, L. N.; Rand, B. P.; Friend, R. H.; Mhaisalkar, S. G.; Lee, T. W.; Sargent, E. H. Perovskites for Next-Generation Optical Sources. *Chem. Rev.* **2019**, *119* (12), 7444–7477.
- (2) Xing, G.; Mathews, N.; Lim, S. S.; Yantara, N.; Liu, X.; Sabba, D.; Grätzel, M.; Mhaisalkar, S.; Sum, T. C. Low-Temperature Solution-Processed Wavelength-Tunable Perovskites for Lasing. *Nat. Mater.* **2014**, *13* (5), 476–480.
- (3) Fakharuddin, A.; Gangishetty, M. K.; Abdi-Jalebi, M.; Chin, S. H.; bin Mohd Yusoff, A. R.; Congreve, D. N.; Tress, W.; Deschler, F.; Vasilopoulou, M.; Bolink, H. J. Perovskite Light-Emitting Diodes. *Nat. Electron.* **2022**, *5* (4), 203–216.
- (4) Chen, Z.; Hoyer, R. L. Z.; Yip, H. L.; Fiuza-Maneiro, N.; López-Fernández, I.; Otero-Martínez, C.; Polavarapu, L.; Mondal, N.; Mirabelli, A.; Anaya, M.; Stranks, S. D.; Liu, H.; Shi, G.; Xiao, Z.; Kim, N.; Kim, Y.; Shin, B.; Shi, J.; Liu, M.; Zhang, Q.; Fan, Z.; Loy, J. C.; Zhao, L.; Rand, B. P.; Arfin, H.; Saikia, S.; Nag, A.; Zou, C.; Lin, L. Y.; Xiang, H.; Zeng, H.; Liu, D.; Su, S. J.; Wang, C.; Zhong, H.; Xuan, T. T.; Xie, R. J.; Bao, C.; Gao, F.; Gao, X.; Qin, C.; Kim, Y. H.; Beard, M. C. Roadmap on Perovskite Light-Emitting Diodes. *J Phys Photonics* **2024**, *6* (3), 032501.
- (5) Tan, Z. K.; Moghaddam, R. S.; Lai, M. L.; Docampo, P.; Higler, R.; Deschler, F.; Price, M.; Sadhanala, A.; Pazos, L. M.; Credgington, D.; Hanusch, F.; Bein, T.; Snaith, H. J.; Friend, R. H. Bright Light-Emitting Diodes Based on Organometal Halide Perovskite. *Nat. Nanotechnol.* **2014**, *9* (9), 687–692.
- (6) Jiang, J.; Chu, Z.; Yin, Z.; Li, J.; Yang, Y.; Chen, J.; Wu, J.; You, J.; Zhang, X. Red Perovskite Light-Emitting Diodes with Efficiency Exceeding 25% Realized by Co-Spacer Cations. *Adv. Mater.* **2022**, *34* (36), 2204460.
- (7) Bai, W.; Xuan, T.; Zhao, H.; Dong, H.; Cheng, X.; Wang, L.; Xie, R.-J. Perovskite Light-Emitting Diodes with an External Quantum Efficiency Exceeding 30%. *Adv. Mater.* **2023**, *35* (39), 2302283.
- (8) Nong, Y.; Yao, J.; Li, J.; Xu, L.; Yang, Z.; Li, C.; Song, J. Boosting External Quantum Efficiency of Blue Perovskite QLEDs Exceeding 23% by Trifluoroacetate Passivation and Mixed Hole Transportation Design. *Adv. Mater.* **2024**, *36* (27), 1–8.
- (9) Li, X.; Yu, D.; Cao, F.; Gu, Y.; Wei, Y.; Wu, Y.; Song, J.; Zeng, H. Healing All-Inorganic Perovskite Films via Recyclable Dissolution–Recrystallization for Compact and Smooth Carrier Channels of Optoelectronic Devices with High Stability. *Adv. Funct. Mater.* **2016**, *26* (32), 5903–5912.
- (10) Wang, W.; Wu, Z.; Ye, T.; Ding, S.; Wang, K.; Peng, Z.; Sun, X. W. High-Performance Perovskite Light-Emitting Diodes Based on Double Hole Transport Layers. *J. Mater. Chem. C* **2021**, *9* (6), 2115–2122.
- (11) Yoon, S. B.; Hwang, S.; Kim, Y.; Kim, B. G.; Na, H. B. Preparation of Water-Dispersible Perovskite-Quantum Dots for Biomedical Applications. *Korean J. Chem. Eng.* **2024**, *41* (13), 3345–3357.
- (12) Shin, M.; Lee, H. S.; Sim, Y. C.; Cho, Y. H.; Cheol Choi, K.; Shin, B. Modulation of Growth Kinetics of Vacuum-Deposited CsPbBr<sub>3</sub> Films for Efficient Light-Emitting Diodes. *ACS Appl. Mater. Interfaces* **2020**, *12*, 1944–1952.
- (13) Ye, J.; Byranvand, M. M.; Martínez, C. O.; Hoyer, R. L. Z.; Saliba, M.; Polavarapu, L. Defect Passivation in Lead-Halide Perovskite Nanocrystals and Thin Films: Toward Efficient LEDs and Solar Cells. *Angew. Chem., Int. Ed.* **2021**, *60*, 21636–21660.
- (14) Park, J.; Cho, H.; Kim, J.; Huang, Y.; Kim, N.; Park, S.; Kim, Y.; Lee, S.; Kwon, J.; Lee, D. C.; et al. Efficient and spectrally stable pure blue light-emitting diodes enabled by phosphonate passivated CsPbBr<sub>3</sub> nanoplatelets with conjugated polyelectrolyte-based energy transfer layer. *EcoMat* **2024**, *6*, No. e12487.
- (15) Chu, S.; Chen, W.; Fang, Z.; Xiao, X.; Liu, Y.; Chen, J.; Huang, J.; Xiao, Z. Large-Area and Efficient Perovskite Light-Emitting Diodes via Low-Temperature Blade-Coating. *Nat. Commun.* **2021**, *12* (1), 147.
- (16) Ban, M.; Zou, Y.; Rivett, J. P. H.; Yang, Y.; Thomas, T. H.; Tan, Y.; Song, T.; Gao, X.; Credgington, D.; Deschler, F.; Siringhaus, H.; Sun, B. Solution-Processed Perovskite Light Emitting Diodes with Efficiency Exceeding 15% through Additive-Controlled Nanostructure Tailoring. *Nat. Commun.* **2018**, *9* (1), 3892.
- (17) Koh, J.; Kim, D.; Park, S. W.; Kim, H.; Hong, K. H.; Shin, B. Selective Reactivity-Assisted Sacrificial Additive Coating for Surface Passivation of Wide Bandgap Perovskite Solar Cells with Cesium Tetrafluoroborate. *J. Mater. Chem. A* **2024**, *12* (7), 4290–4298.
- (18) Li, J.; Bade, S. G. R.; Shan, X.; Yu, Z. Single-Layer Light-Emitting Diodes Using Organometal Halide Perovskite/Poly-(Ethylene Oxide) Composite Thin Films. *Adv. Mater.* **2015**, *27* (35), 5196–5202.
- (19) Yuan, S.; Cui, L. S.; Dai, L.; Liu, Y.; Liu, Q. W.; Sun, Y. Q.; Auras, F.; Anaya, M.; Zheng, X.; Ruggeri, E.; Yu, Y. J.; Qu, Y. K.; Abdi-Jalebi, M.; Bakr, O. M.; Wang, Z. K.; Stranks, S. D.; Greenham, N. C.; Liao, L. S.; Friend, R. H. Efficient and Spectrally Stable Blue Perovskite Light-Emitting Diodes Employing a Cationic  $\pi$ -Conjugated Polymer. *Adv. Mater.* **2021**, *33*, 2103640.
- (20) Liu, Z.; Qiu, W.; Peng, X.; Sun, G.; Liu, X.; Liu, D.; Li, Z.; He, F.; Shen, C.; Gu, Q.; Ma, F.; Yip, H. L.; Hou, L.; Qi, Z.; Su, S. J. Perovskite Light-Emitting Diodes with EQE Exceeding 28% through a Synergistic Dual-Additive Strategy for Defect Passivation and Nanostructure Regulation. *Adv. Mater.* **2021**, *33* (43), 1–9.
- (21) Ma, D.; Lin, K.; Dong, Y.; Choubisa, H.; Proppe, A. H.; Wu, D.; Wang, Y. K.; Chen, B.; Li, P.; Fan, J. Z.; Yuan, F.; Johnston, A.; Liu, Y.; Kang, Y.; Lu, Z. H.; Wei, Z.; Sargent, E. H. Distribution Control Enables Efficient Reduced-Dimensional Perovskite LEDs. *Nature* **2021**, *599* (7886), 594–598.
- (22) Li, J.; Du, P.; Guo, Q.; Sun, L.; Shen, Z.; Zhu, J.; Dong, C.; Wang, L.; Zhang, X.; Li, L.; Yang, C.; Pan, J.; Liu, Z.; Xia, B.; Xiao, Z.; Du, J.; Song, B.; Luo, J.; Tang, J. Efficient All-Thermally Evaporated Perovskite Light-Emitting Diodes for Active-Matrix Displays. *Nat. Photonics* **2023**, *17* (5), 435–441.
- (23) Qin, F.; Tian, H.; Yan, M.; Fang, Y.; Yang, D. Cesium-Lead-Bromide Perovskites with Balanced Stoichiometry Enabled by Sodium-Bromide Doping for All-Vacuum Deposited Silicon-Based Light-Emitting Diodes. *J. Mater. Chem. C* **2021**, *9* (6), 2016–2023.
- (24) Fu, Y.; Zhang, Q.; Zhang, D.; Tang, Y.; Shu, L.; Zhu, Y.; Fan, Z. Scalable All-Evaporation Fabrication of Efficient Light-Emitting Diodes with Hybrid 2D–3D Perovskite Nanostructures. *Adv. Funct. Mater.* **2020**, *30*, 2002913.
- (25) Peng, C.; Chen, B.; Liu, X.; Guo, R.; He, Z.; Zhang, F.; He, X.; Sun, L.; Liu, Z.; Xiong, Y.; Gao, F.; Wang, L. High-Performance Thermally Evaporated Blue Perovskite Light-Emitting Diodes Enabled by Post-Evaporation Passivation. *Chem. Eng. J.* **2024**, *499* (August), 155955.
- (26) Veeramuthu, L.; Liang, F. C.; Zhang, Z. X.; Cho, C. J.; Ercan, E.; Chueh, C. C.; Chen, W. C.; Borsali, R.; Kuo, C. C. Improving the Performance and Stability of Perovskite Light-Emitting Diodes by a

Polymeric Nanothick Interlayer-Assisted Grain Control Process. *ACS Omega* **2020**, *5* (15), 8972–8981.

(27) Shin, M.; Nam, S. W.; Sadhanala, A.; Shivanna, R.; Anaya, M.; Jiménez-Solano, A.; Yoon, H.; Jeon, S.; Stranks, S. D.; Hoye, R. L. Z.; Shin, B. Understanding the Origin of Ultrasharp Sub-Bandgap Luminescence from Zero-Dimensional Inorganic Perovskite Cs<sub>4</sub>PbBr<sub>6</sub>. *ACS Appl. Energy Mater.* **2020**, *3*, 192.

(28) Du, P.; Li, J.; Wang, L.; Sun, L.; Wang, X.; Xu, X.; Yang, L.; Pang, J.; Liang, W.; Luo, J.; Ma, Y.; Tang, J. Efficient and Large-Area All Vacuum-Deposited Perovskite Light-Emitting Diodes via Spatial Confinement. *Nat. Commun.* **2021**, *12* (1), 1–10.

(29) Hu, Y.; Wang, Q.; Shi, Y. L.; Li, M.; Zhang, L.; Wang, Z. K.; Liao, L. S. Vacuum-Evaporated All-Inorganic Cesium Lead Bromine Perovskites for High-Performance Light-Emitting Diodes. *J. Mater. Chem. C* **2017**, *5* (32), 8144–8149.

(30) Chen, B.; Peng, C.; Guo, R.; He, Z.; Sun, L.; Zhang, F.; He, X.; Zeng, H.; Wang, L. Dual-Function Self-Assembled Molecules as Hole-Transport Layers for Thermally Evaporated High-Efficiency Blue Perovskite Light-Emitting Diodes. *Adv. Mater.* **2025**, *37* (3), 2411451.

(31) Zhu, L.; Liu, D.; Wang, J.; Wang, N. Large Organic Cations in Quasi-2D Perovskites for High-Performance Light-Emitting Diodes. *J. Phys. Chem. Lett.* **2020**, *11* (20), 8502–8510.

(32) Zhang, L.; Sun, C.; He, T.; Jiang, Y.; Wei, J.; Huang, Y.; Yuan, M. High-Performance Quasi-2D Perovskite Light-Emitting Diodes: From Materials to Devices. *Light: Sci. Appl.* **2021**, *10* (1), 61.

(33) Yuan, M.; Quan, L. N.; Comin, R.; Walters, G.; Sabatini, R.; Voznyy, O.; Hoogland, S.; Zhao, Y.; Beaugregard, E. M.; Kanjanaboos, P.; Lu, Z.; Kim, D. H.; Sargent, E. H. Perovskite Energy Funnels for Efficient Light-Emitting Diodes. *Nat. Nanotechnol.* **2016**, *11* (10), 872–877.

(34) Ng, Y. F.; Kulkarni, S. A.; Parida, S.; Jamaludin, N. F.; Yantara, N.; Bruno, A.; Soci, C.; Mhaisalkar, S.; Mathews, N. Highly Efficient Cs-Based Perovskite Light-Emitting Diodes Enabled by Energy Funnelling. *Chem. Commun.* **2017**, *53* (88), 12004–12007.

(35) Gil, B.; Kim, J.; Park, B. Phenyltrimethylammonium as an Interlayer Spacer for Stable Formamidinium-Based Quasi-2D Perovskite Solar Cells. *Electron. Mater. Lett.* **2024**, *20*, 791–798.

(36) Park, S.; Kim, J.; Kim, G. M.; Park, J.; Lee, S.; Lee, D. C.; Kim, N.; Cho, B. G.; Shin, B. Controlling the Phase Distribution of Single Bromide Quasi-2-Dimensional Perovskite Crystals via Solvent Engineering for Pure-Blue Light-Emitting Diodes. *ACS Appl. Mater. Interfaces* **2024**, *16* (29), 38395–38403.

(37) Vashishtha, P.; Ng, M.; Shivarudraiah, S. B.; Halpert, J. E. High Efficiency Blue and Green Light-Emitting Diodes Using Ruddlesden-Popper Inorganic Mixed Halide Perovskites with Butylammonium Interlayers. *Chem. Mater.* **2019**, *31* (1), 83–89.

(38) Hsieh, C.-A.; Tan, G.-H.; Chuang, Y.-T.; Lin, H.-C.; Lai, P.-T.; Jan, P.-E.; Chen, B.-H.; Lu, C.-H.; Yang, S.-D.; Hsiao, K.-Y.; Lu, M.-Y.; Chen, L.-Y.; Lin, H.-W. Vacuum-Deposited Inorganic Perovskite Light-Emitting Diodes with External Quantum Efficiency Exceeding 10% via Composition and Crystallinity Manipulation of Emission Layer under High Vacuum. *Adv. Sci.* **2023**, *10* (10), 2206076.

(39) Kim, N.; Shin, M.; Jun, S.; Choi, B.; Kim, J.; Park, J.; Kim, H.; Jung, W.; Lee, J. Y.; Cho, Y. H.; Shin, B. Highly Efficient Vacuum-Evaporated CsPbBr<sub>3</sub> Perovskite Light-Emitting Diodes with an Electrical Conductivity Enhanced Polymer-Assisted Passivation Layer. *ACS Appl. Mater. Interfaces* **2021**, *13* (31), 37323–37330.

(40) Zheng, G.; Zhu, C.; Ma, J.; Zhang, X.; Tang, G.; Li, R.; Chen, Y.; Li, L.; Hu, J.; Hong, J.; Chen, Q.; Gao, X.; Zhou, H. Manipulation of Facet Orientation in Hybrid Perovskite Polycrystalline Films by Cation Cascade. *Nat. Commun.* **2018**, *9* (1), 1–11.

(41) Yoon, H.; Hong, S.; Lee, S. H.; Cho, I. H.; Kim, H. J. GIWAXS Analysis on Preferred Orientation in Metal Halide Perovskite Films Via Alkylamines. *Electron. Mater. Lett.* **2022**, *18* (5), 456–464.

(42) Zhang, Y.; Wang, Z.; Liu, T.; Yang, B.; Hu, S.; Li, H.; Sheng, C. X. Effects of Spin-Casting Speed on Solar Cell Performances and Corresponding Films Morphology and Optical Properties Using 2D Perovskite of PEA<sub>2</sub>MA<sub>2</sub>Pb<sub>3</sub>I<sub>10</sub>. *Electron. Mater. Lett.* **2022**, *18* (3), 282–293.

(43) Kim, D.; Jung, H. J.; Park, I. J.; Larson, B. W.; Dunfield, S. P.; Xiao, C.; Kim, J.; Tong, J.; Boonmongkolras, P.; Ji, S. G.; Zhang, F.; Pae, S. R.; Kim, M.; Kang, S. B.; Dravid, V.; Berry, J. J.; Kim, J. Y.; Zhu, K.; Kim, D. H.; Shin, B. Efficient, Stable Silicon Tandem Cells Enabled by Anion-Engineered Wide-Bandgap Perovskites. *Science* **2020**, *368* (6487), 155–160.

(44) Bube, R. H. Trap Density Determination by Space-Charge-Limited Currents. *J. Appl. Phys.* **1962**, *33* (5), 1733–1737.



CAS BIOFINDER DISCOVERY PLATFORM™

**PRECISION DATA  
FOR FASTER  
DRUG  
DISCOVERY**

CAS BioFinder helps you identify targets, biomarkers, and pathways

**Unlock insights**

**CAS**  
A Division of the  
American Chemical Society